Experimental and numerical investigations of snow accretion

Boris Aguilar, Kilian Köbschall, Louis Reitter, Pierre Trontin, Fabien Dezitter, Jan Breitenbach, Ilia Roisman, Olivier Rouzaud, Philippe Villedieu

Experimental and numerical investigations of snow accretion

B. Aguilar [a*], K. Köbschall [b], L. Reitter [b], P. Trontin [c], F. Dezitter [a], J. Breitenbach [b], I. Roisman [b], O. Rouzaud [c], P. Villedieu [c]

[a] *Airbus Helicopters S.A.S. - Aéroport International Marseille-Provence - 13725 Marignane Cedex - France*

[b] *Technische Universität Darmstadt, Institute for Fluid Mechanics and Aerodynamics, Alarich-Weiss-Straße 10, 64287 Darmstadt, Germany*

[c] *ONERA/DMPE, Université de Toulouse, F-31055 Toulouse, France*

To ensure safe flight under snowy conditions, aircraft manufacturers must demonstrate that each engine and its air inlet system can operate throughout the flight power range of the engine (including idling) in snow, both falling and blowing. This study is part of an effort to develop models for snow accretion. More specifically, the focus is on the transport step, taking into account both dynamic aspects (with the estimation of the particle trajectory) and thermal effects (with possible melting of snow crystals/snowflakes). Experiments and numerical simulations are compared for the estimation of the drag coefficient in the context of a free falling snowflake. Thermal effects observed during the melting of a snowflake in forced convection are also studied.

Nomenclature

m	=	Mass
d_{eq}	=	Volume equivalent diameter
$\boldsymbol{v}$	=	Velocity
$\boldsymbol{w}$	=	Relative velocity between air and particle
$\boldsymbol{F}_{\mathrm{D}}$	=	Drag force
C_{D}	=	Drag coefficient
Re	=	Reynolds number
ρ	=	Density
μ	=	Dynamic viscosity
A	=	Surface
T	=	Temperature
Φ	=	Sphericity
$\Phi^{\perp}$	=	Crosswise sphericity
$A^{\perp}$	=	Projected surface of the particule normal to the airflow
k	=	Heat conductivity
L	=	Latent heat
D	=	Diffusivity
c_p	=	Specific heat capacity
Sh	=	Sherwood number
Sc	=	Schmidt number
Pr	=	Prandtl number
e	=	Spheroid eccentricity

Subscripts

p	=	Particle
a	=	Air
i	=	Ice
w	=	Water

*Corresponding author: boris.aguilar@airbus.com

v = Vapour/Vaporization
0 = Initial value

Introduction

To ensure safe flight under snowy conditions, aircraft manufacturers must demonstrate that each engine and its air inlet system can operate throughout the flight power range of the engine (including idling) in snow, both falling and blowing, without adverse effect on engine operation (power or thrust loss, surge, stall or flameout).

Snow particles are precipitation sized ice particles that form in clouds and precipitate to the ground. Falling snow formation has its origin in a complex interplay of microphysical processes and properties (vapor deposition, riming, and aggregation, hydrometeor fall speed), which are governed by cloud dynamics (vertical and horizontal transport) and thermodynamics (temperature and humidity vertical profiles). Snow particles have interested scientists since a long time and the first systematic studies of snow crystals started with the pioneering work of Nakaya [1]. Numerous studies about snow particles have been published in contemporary literature since these early studies. The terminology of Pruppacher and Klett [2] is adopted here: ice particles grown by vapor deposition and/or riming are called snow crystals and aggregates of snow crystals are referred to as snowflakes.

Due to the variability of atmospheric conditions prevailing in snow clouds, the shape, size, density, and related properties such as drag and terminal fall speed of natural snow particles (snow crystal and snowflakes) are found to be highly variable. Regarding the shape for instance, Fig. 1 presents samples of ice crystals (columns, columns with plates, plates in the top row, planar dendrites in the third row, graupel (or snow pellets) in the fifth row) and snowflakes with different degrees of riming in the three last rows. This point was not addressed by the European projects HAIC [4] and

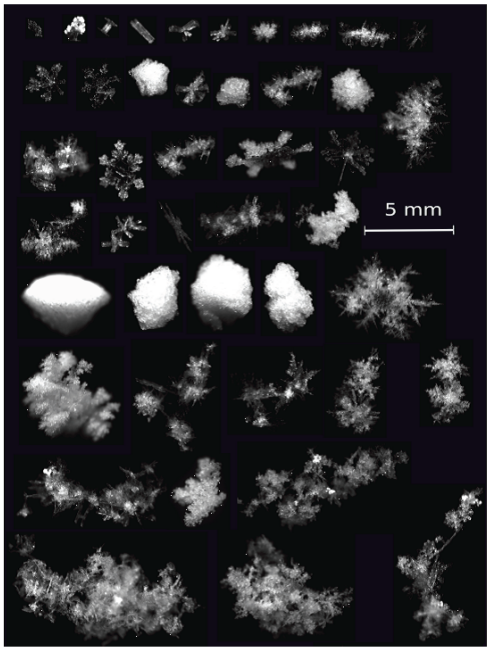

Fig. 1 MASC picture of hydrometeor illustrating the variability in the shape and size of snow particles [3].

MUSIC-haic [5], where the models for trajectory, impact and erosion [6–22] were derived for ice particles with higher densities and more regular geometric shapes. In the framework of these two previous projects [4, 5], models for mixed phase and ice crystal icing (Appendix D) have been derived from academic [10, 16] and more applied experiments [11, 15] to be integrated into numerical tools able to simulate the entire accretion process [14]. However, regarding the risk of snow accretion or accumulation, there are currently no validated engineering tools (test facility and numerical tools) available. This is one of the main objectives of the European project ICE-GENESIS [23].

This study is part of an effort to develop models for snow accretion. More specifically, the focus is on the transport step, taking into account both dynamic aspects (with the estimation of the particle trajectory) and thermal effects (with

possible melting of snow crystals/snowflakes). In a first part, two experiments are detailed. The first one is dedicated to the measurement of the drag coefficient of a free falling snowflake. The second one is related to the melting of a snowflake in forced convection. The procedure for post-processing images generated by the experiments is also described. The second part presents the derivation of the models for the drag coefficient and the melting process adapted to snowflakes. A comparison between the experiments and the numerical simulations is drawn in the third part. Finally, conclusions are given.

I. Experiments: free fall and melting of a snowflake

A. Experimental Apparatus

For the experiments, artificial snowflakes are used. However, these artificial snowflakes are close to natural snowflakes like those depicted in Fig. 1.

1. Free fall experiment

The experimental setup used for the measurement of snowflake drag is schematically shown in Fig. 2. The entire

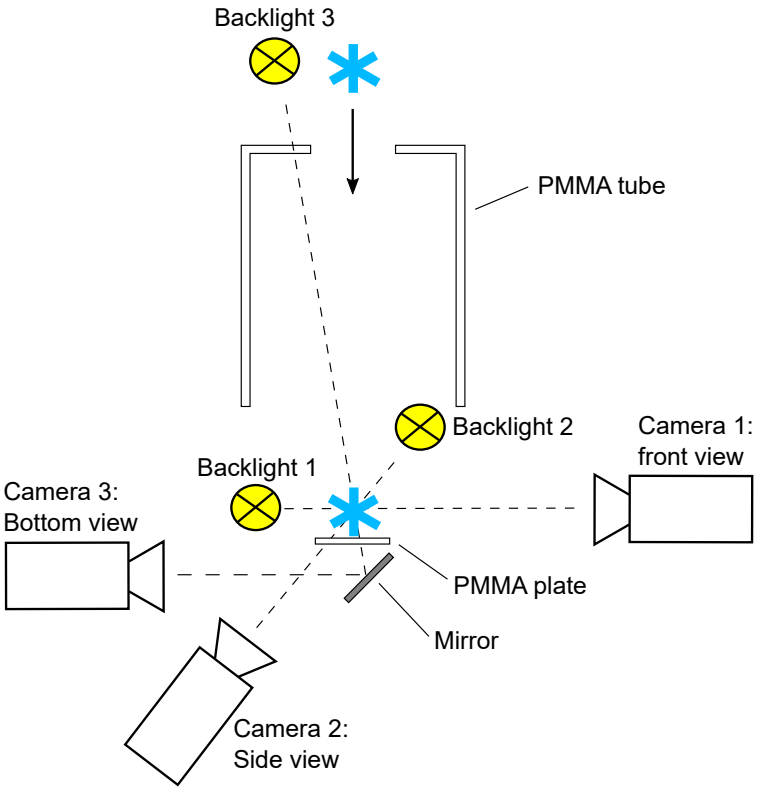

Fig. 2 Schematic view of the experimental setup used to measure snowflake drag.

setup and measurement equipment is mobile and can be operated at ambient temperatures down to −20 °C. The setup consists of a large PMMA tube with a diameter and height of 150 mm and 300 mm, respectively. Through a baffle (opening of 10 mm) at its top, free falling snowflakes enter the PMMA tube, which has the purpose of shielding them from possible external gusts influencing their trajectory. Immediately after a snowflake falls out of the PMMA tube, its movement is captured using high-speed cameras in a front, side and bottom view. The resolutions of the front, side and bottom views are 24.1 µm/pixel , 34.6 µm/pixel and 51.7 µm/pixel, respectively. The side view has the largest field of view and is primarily used for measuring the free fall velocity. After the measurement of their terminal velocity, the snowflakes are caught and melted on a transparent, superhydrophobic coated PMMA plate, forming nearly spherical liquid drops. These drops are captured using the front view camera, which allows measurement of the drop diameter

and therefore, the computation of the snowflake mass. Measurement of the snowflake projected area in three nearly orthogonal views, as well as measuring their mass, allows the calculation of the snowflake drag coefficient corresponding to its characteristic terminal velocity. Figure 3 shows example images of a snowflake in the front view, falling with a terminal velocity of 1.36 m/s and finally landing on the PMMA plate. As shown in Fig. 3, a snowflake might be very

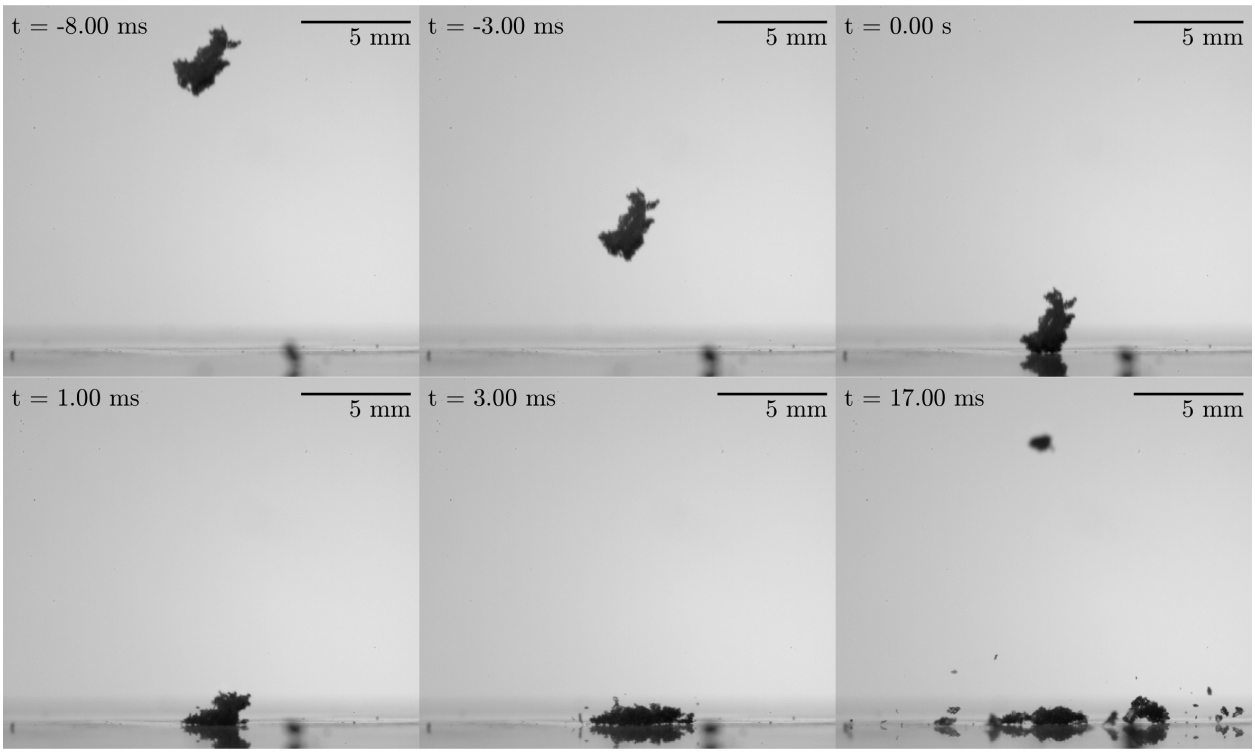

Fig. 3 Example images of a snowflake recorded with camera 1 (front view) having a resolution of 24.1 µm/pixel. The snowflake's maximum dimension is 3.5 mm and its terminal velocity is 1.36 m/s.

fragile and shatters when it impinge the PMMA plate, even if it falls with a rather moderate terminal velocity. In the case of fragmentation, all fragments are collected and melted together, using a stream of hot air directed toward the bottom of the PMMA plate. As a result, an almost spherical drop is formed on top of the superhydrophobic PMMA plate, an example which can be seen in Fig. 4. The diameter of the drop is 0.795 mm and its mass is computed as 0.263 mg.

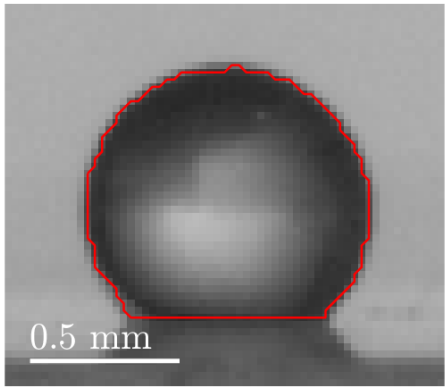

Fig. 4 Image of the melted snowflake, having a mass of 0.263 mg and a diameter of 0.795 mm.

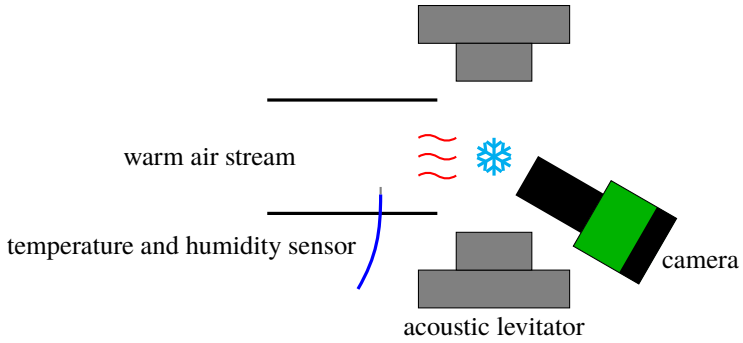

Fig. 5 The setup for the experimental investigation of the melting of single snowflakes in forced convection.

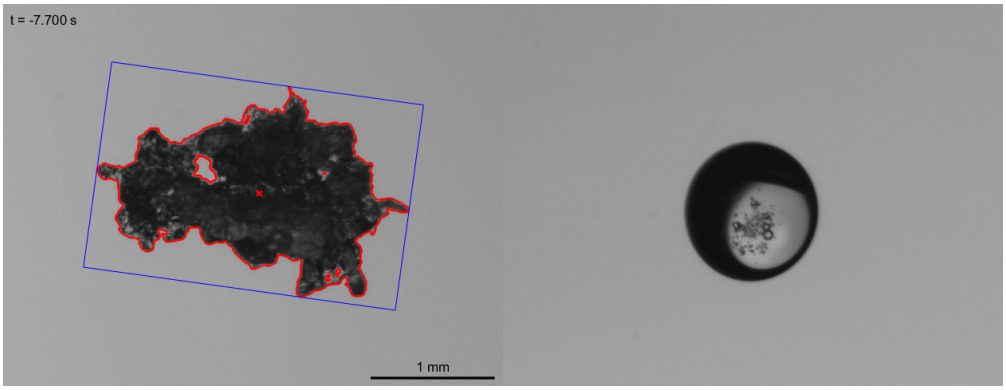

(a) Before melting (b) After melting

Fig. 6 Exemplary snowflake before melting levitating in the acoustic levitator and resulting drop with enclosed air bubbles.

Using the snowflake images of the front, side and bottom view, characteristic size and shape parameters can be derived.

2. Melting

A setup for the experimental investigation of the melting of single snowflakes has been developed that enables the observation of melting snowflakes in forced convection. The setup is built such that it prevents the melting flakes from having contact to any solid structure and thus, simulates the melting in falling or blowing snow conditions. Figure 5 illustrates the setup. Its main component is the acoustic levitator, which utilizes a standing ultrasonic wave to levitate the snowflake. The snowflakes are caught with a nylon net and placed into the acoustic levitator. A warm air stream, well defined in terms of temperature, humidity and volume flow rate, is then used to melt the snowflake. The melting processes as well as the size of the melted snowflake are captured in a side-view using a high-resolution video camera. The warm air flow is provided by a controllable hot air blower attached to a pipe. In this pipe, shortly before the exit, the temperature and humidity of the air flow are measured. The hot air blower runs for a sufficient duration for the device and the pipe to heat up and reach steady state. During this period, the warm air is not directed toward the snowflake, but is redirected through a hose.

Due to the irregular shape of the snowflakes, their orientation in the acoustic levitator was rather instable. Consequentially, snowflakes were often ejected out of the levitator and it proved difficult to adjust the settings to observe them throughout the full melting process. An exemplary photograph of a snowflake before melting is shown in Fig. 6a.

When no more ice is visible in the liquid drop, the volume of the drop is calculated by rotating the projected shape. The volume of the drop is taken to estimate the initial mass of the snowflake. Finally, the time it takes for the snowflake to melt is determined by finding the first image in which no residual ice can be detected.

As soon as the flake is exposed to the warm airflow, its arms start to melt and the melt water is drawn to the flake

centre due to surface tension. This results in a decrease in the visible size. This decrease flattens when the snowflake arms are melted and the remaining ice and water form a more compact shape. This transformation to a more compact shape results in a more spherical shape. The melt water then forms a drop, which completely encloses the remaining ice. In many cases, small bubbles of air can be observed in the resulting liquid drop, which then coalesce. An exemplary drop with enclosed air bubbles is shown in Fig. 6b.

B. Image post-processing

In this part we briefly present the processing of the images acquired during the experiments described in section I.A.1. Umbroscopic measurements provide grayscale or black and white images of the projected surface in the direction of the camera. An image processing tool has been developed to provide the maximum f_{max} and maximum orthogonal $f^{\perp}_{max}$ diameters of Feret ($f^{\perp}_{max}$ is defined as the largest diameter among all diameters orthogonal to f_{max}, in green in Fig. 7b). It should be noted that $A^{\perp}$ is almost never the projected area perpendicular to the flow. It has been chosen to ensure consistrency with the definition usually found in the literature but in practice it is often not possible to know the direction of the flow with respect to the image. Using Feret's diameters it can be deduced an ellipse of major semi axis $a = \mathrm{f_{max}}/2$ and minor semi axis $\mathrm{f^{\perp}_{max}}/2$. From the axes of the ellipse we can construct either an oblate spheroid or a

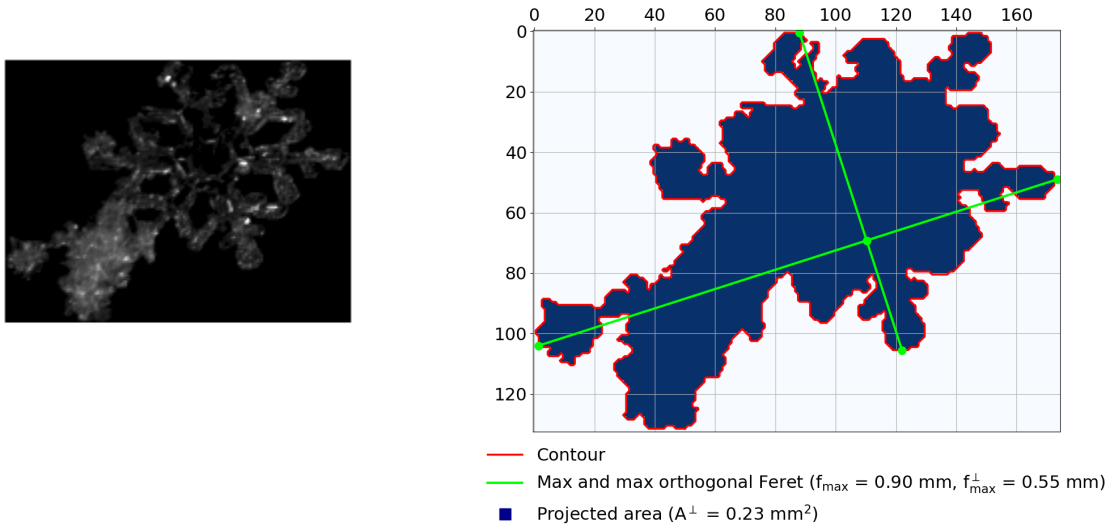

(a) Grayscale image of a snowflake

(b) Post processed image

Fig. 7 Data post-processing illustration

prolate spheroid of volume $V_{\mathrm{spheroid}} = \pi/6A^2C$. For an oblate spheroid $A = 2a$ and $C = 2c$. For a prolate spheroid $A = 2c$ and $C = 2a$. Using these parameters, the following characteristics can be deduced:

$$d_{\mathrm{V}} = \left(\frac{6V_{\mathrm{spheroid}}}{\pi}\right)^{1/3}, \quad \Phi = \frac{\pi d_{\mathrm{V}}^2}{A_{\mathrm{spheroid}}}, \quad \Phi^{\perp} = \frac{\frac{\pi}{4}d_{\mathrm{V}}^2}{A^{\perp}}, \quad Re_p = \frac{\rho_{\mathrm{a}} w d_{\mathrm{V}}}{\mu_{\mathrm{a}}} \tag{1}$$

where $A_{\mathrm{spheroid}} = 2\pi a^2 + \pi\frac{c^2}{e}\ln\left(\frac{1+e}{1-e}\right)$ for an oblate spheroid and $A_{\mathrm{spheroid}} = 2\pi a^2\left(1 + \frac{c}{ae}\arcsin e\right)$ for a prolate spheroid. The eccentricity of the ellipse is written $e = 1 - \frac{a^2}{c^2}$.

The test case configurations for the snowflake free fall study (Sec. I.A.1) are summarized in Tab. 1. Regarding the melting experiment (Sec. I.A.2), the configurations are given in Tab. 3.

II. Models for particle trajectory and melting

A. Snow particle trajectory

For the computation of the snow particle trajectory, since snow particle density is much higher than air density, it is possible to neglect the influences of the virtual mass force, the Basset force, the pressure gradient force and the lift force compared to the drag force in the momentum equation. Hence, the particle motion equation simply reads:

$$m_\mathrm{p}\frac{\mathrm{d}\boldsymbol{v}_\mathrm{p}}{\mathrm{d}t} = \boldsymbol{F}_\mathrm{D} + m_\mathrm{p}\boldsymbol{g}, \quad \boldsymbol{F}_\mathrm{D} = -\frac{1}{2}\rho_\mathrm{a}||\boldsymbol{w}||\boldsymbol{w}A_\mathrm{ref}C_\mathrm{D,ref}(Re_\mathrm{p}) \tag{2}$$

where m_p is the snow particle mass, $\boldsymbol{v}_\mathrm{p}$ its velocity, $\boldsymbol{F}_\mathrm{D}$ the drag force, $\boldsymbol{g}$ the gravity, ρ_a the air density and $\boldsymbol{w} = \boldsymbol{v}_\mathrm{p} - \boldsymbol{v}_\mathrm{a}$ denotes the relative velocity between air and the particle. In the following, $||\boldsymbol{w}||$ will simply be denoted w. The drag coefficient $C_\mathrm{D,ref}$ is defined with respect to the reference surface A_ref. It is a function of the particle Reynolds number $Re_\mathrm{p} = \frac{\rho_\mathrm{a} w d_\mathrm{ref}}{\mu_\mathrm{a}}$ where μ_a is the air dynamic viscosity, d_ref a characteric length scale and ρ_a the air density. Note that in the case of a snowflake with a complex shape (for instance aggregates, see Fig. 1) the definition of ρ_p has to be specified and may refer to the bulk density for instance.

Two sets of definitions will be used to define ρ_p, d_ref, A_ref and $C_\mathrm{D,ref}$. The first one is drawn from the Hölzer and Sommerfeld correlation [24] for non-spherical particles (section II.A.1). The second one is obtained from the Heymsfield and Westbrook modeling [25] (section II.A.2).

1. The Hölzer and Sommerfeld model [24]

Among the several general expressions that can be found in the literature for the expression of the drag coefficient $C_\mathrm{D,ref}$ for non-spherical particles, we can mention the models of Haider *et al.* [26], Ganser [27] and Hölzer *et al.* [24]. For these models, d_V is the volume equivalent diameter $d_V = \left(\frac{6V_\mathrm{p}}{\pi}\right)^{1/3}$ of a sphere having the same volume V_p as the non-spherical particle. The reference surface is defined as $A_\mathrm{ref} = \pi d_V^2/4$.

The Hölzer *et al.* model has been selected in this study since it is valid for a wide range of shapes. Moreover, compared to the Haider *et al.* and Ganser models, it is based on the influence of the crosswise sphericity in the asymptotic expression of the drag coefficient in the Newton regime . This regime is typical for accretion scenarios during helicopter flight.

For the Hölzer and Sommerfeld model [24], the drag coefficient can be written:

$$C_\mathrm{D,ref} = \frac{8}{Re_\mathrm{p}\sqrt{\Phi_\perp}} + \frac{16}{Re_\mathrm{p}\sqrt{\Phi}} + \frac{3}{\sqrt{Re_\mathrm{p}}\Phi^{0.75}} + \frac{0.421}{\Phi_\perp}10^{0.4(-\log\Phi)^{0.2}} \tag{3}$$

Sphericity Φ and crosswise sphericity $\Phi^\perp$ are defined as:

$$\Phi = \frac{\pi d_\mathrm{V}^2}{A_\mathrm{spheroid}}, \quad \Phi^\perp = \frac{\frac{\pi}{4}d_\mathrm{V}^2}{A^\perp} \tag{4}$$

where A_spheroid denotes the surface of the approximated spheroid and $A^\perp$ is the projected surface of the particle in the considered view.

In practice, the volume V_p is not obtained directly from the experimental data. This is why V_p is estimated from a reconstructed oblate or prolate spheroid from planar images of the particle. It should also be noted that the density of the particle becomes a bulk density defined as the mass contained in the spheroid:

$$\rho_p = \frac{m_\mathrm{p}}{V_\mathrm{Spheroid}} \tag{5}$$

where m_p is the mass of the particle that has to be provided either by the experiments or by a correlation (Baker and Lawson [28]). The procedure is detailed in Sec. I.B.

2. The Heymsfield and Westbrook model [25]

The second model studied is that of Heymsfield and Westbrook [25], which is an improvement of the models based on the Abraham's drag coefficient of a sphere[29].

The Abraham model for spherical particles In Abraham [29], the problem is considered as an assembly of a smooth sphere of radius a plus a thin boundary layer of thickness δ in a moving fluid of density ρ_a at a velocity v. The assembly is then assumed to evolve in an asymptotic low viscosity aerodynamic flow in a regime where the drag coefficient is independant of Re_p. These assumptions lead to the following expression for the drag force of a sphere of radius $a + \delta$:

$$F_D = \frac{\rho_a v^2}{2} \pi (a + \delta)^2 C_{D0} \tag{6}$$

where C_{D0} is a constant parameter to be adjusted. Equation (7) may be re-written as:

$$F_D = \frac{\rho_a v^2}{2} \pi a^2 C_{D0} \left(1 + \frac{\delta}{a}\right)^2 \tag{7}$$

which is the drag force for the particle of radius a with $C_{D0}\left(1 + \frac{\delta}{a}\right)^2$ as drag coefficient. The boundary layer thickness is given by $\frac{\delta}{a} = \frac{\delta_0}{\sqrt{Re_p}}$ where δ_0 is a dimensionless coefficient. This leads to the following drag coefficient definition for the particle:

$$C_D = C_{D0} \left[1 + \frac{\delta_0}{\sqrt{Re_p}}\right]^2 \tag{8}$$

where C_{D0} and δ_0 are taken to ensure $C_{D0}\delta_0^2 = 24$ (Stokes regime) and $\delta_0 = 9.06$.

Extension to non-spherical particles Many authors have used this relationship for non-spherical particles. In the case of free fall, one can rewrite Eq. (2) alongside the direction of fall with the Best or Davies number:

$$X = C_{d,ref} Re_p^2 = \frac{2 m_p g \rho_a d_{ref}^2}{\mu_a^2 A_{ref}} \tag{9}$$

The corresponding $Re_p(X)$ relationship is given by Bohm [30]:

$$Re_p = \frac{\delta_0^2}{4} \left[\left(1 + \frac{4\sqrt{X}}{\delta_0^2 \sqrt{C_{D0}}}\right)^{1/2} - 1 \right]^2 \tag{10}$$

with $C_{D0} = 0.35$ and $\delta_0 = 8$. Choosing $d_{ref} = d_{max}$ as the maximum Feret diameter and $A_{ref} = A^{\perp}$ and introducing the area ratio, which is the ratio of the particle's projected area to the area of a circumscribing circle $A_r = \frac{A^{\perp}}{\pi d_{max}^2/4}$, we can write $X = \frac{8 m_p g \rho_a}{\mu_a^2 \pi A_r}$. Mitchell, Heymsfield, Khvorostyanov and Curry (MHKC) [31–35] used this method to calculate the drag coefficient and compared the resulting fall velocities to a very wide range of particles. Planar and columnar-type, graupel and aggregates with a size range from 250 µm to 8 mm were studied. More recently, Heymsfield and Westbrook found that fall velocity estimates were overestimated for particles with a low area ratio. In some cases the relative error exceeded 100 % and this effect appears to be strongest at low Reynolds number. Needles, dendrites, stellars and aggregates are key particle types that are affected by this bias. To mitigate this high sensitivity to the area ratio, they considered the following modified drag coefficient:

$$C_D^* = C_D A_r^{1/2}, \quad X^* = \frac{8 \rho_a m_p g}{\mu_a^2 \pi A_r^{1/2}}, \quad Re_p = \frac{\delta_0^2}{4} \left[\left(1 + \frac{4\sqrt{X^*}}{\delta_0^2 \sqrt{C_{D0}}}\right)^{1/2} - 1 \right]^2 \tag{11}$$

In this model, the density ρ_p is defined as:

$$\rho_p = \frac{m_p}{\pi d_{max}^3/6} \tag{12}$$

The particle mass m_p may be obtained either from an experimental measurement or, if not available, from an empirical mass-diameter correlation.

B. Snow particle melting

For the sake of completeness, the model is briefly described in this section. For a more detailed description, see [12]. The general form of the heat equation reads:

$$m_\mathrm{p} c_\mathrm{p,i} \frac{\mathrm{d}T_\mathrm{p}}{\mathrm{d}t} = A_\mathrm{p} h_t (T_\mathrm{a} - T_\mathrm{p}) - \dot{m}_\mathrm{ev} L_\mathrm{v}(T_\mathrm{p}) - \dot{m}_\mathrm{sub} L_\mathrm{s}(T_\mathrm{p}) - \dot{m}_\mathrm{f} L_\mathrm{f}(T_\mathrm{p}) \tag{13}$$

where $c_\mathrm{p,i}$ denotes the specific heat capacity of the ice, T_p is the particle temperature (supposed to be almost uniform inside the particle), h_t is the mean heat transfer coefficient and T_a is the air temperature. L_v, L_s and L_f are respectively the latent heat of evaporation, sublimation and fusion. $\dot{m}_\mathrm{f}$ is the melting rate. The evaporation and sublimation rates ($\dot{m}_\mathrm{ev}$ and $\dot{m}_\mathrm{sub}$)) can be written as:

$$\dot{m}_\mathrm{ev} = \rho_\mathrm{a} A_\mathrm{p} h_m (y_\mathrm{v,s}^\mathrm{liq}(T_\mathrm{p}, p_\mathrm{a}) - y_{\mathrm{v},\infty}) \tag{14a}$$

$$\dot{m}_\mathrm{sub} = \rho_\mathrm{a} A_\mathrm{p} h_m (y_\mathrm{v,s}^\mathrm{sol}(T_\mathrm{p}, p_\mathrm{a}) - y_{\mathrm{v},\infty}) \tag{14b}$$

where h_m is the mean mass transfer coefficient, $y_{\mathrm{v},\infty}$ is the freestream steam mass fraction and $y_\mathrm{v,s}^\mathrm{liq}(T_\mathrm{p}, p_\mathrm{a})$ (resp. $y_\mathrm{v,s}^\mathrm{sol}(T_\mathrm{p}, p_\mathrm{a})$) is the saturated steam mass fraction at the surface of the particle computed above liquid water (resp. solid water). Depending on the particle temperature three cases can be considered:

1) The particle is fully glaciated and its temperature is lower than the melting temperature ($T_\mathrm{p} < T_\mathrm{f}$). There is no melting ($\dot{m}_\mathrm{f} = 0$) and no evaporation ($\dot{m}_\mathrm{ev} = 0$) during this phase.
2) The particle is at the melting temperature ($T_\mathrm{p} = T_\mathrm{f}$). During the melting process the liquid water is assumed to cover the ice core so that there is no sublimation ($\dot{m}_\mathrm{sub} = 0$).
3) The particle is fully liquid and its temperature is larger than the melting temperature ($T_\mathrm{p} > T_\mathrm{f}$). There is no melting ($\dot{m}_\mathrm{f} = 0$) and no sublimation ($\dot{m}_\mathrm{sub} = 0$) during this phase.

Two different models are compared to define h_t and h_m, namely a model based on a modified definition of the Nusselt and Sherwood numbers (II.B.1) and the Mitra's model (II.B.2).

1. Model based on modified Nusselt and Sherwood numbers (mNS moddel)

Introducing the sphericity $\Phi = \frac{\pi d_\mathrm{V}^2}{A_\mathrm{spheroid}}$, the Nusselt number $Nu = \frac{h_t \cdot d_\mathrm{V}}{k_\mathrm{a}}$ and the Sherwood number $Sh = \frac{h_m \cdot d_\mathrm{V}}{D_\mathrm{v,a}}$ where k_a is the air conductivity and $D_\mathrm{v,a}$ is the vapor diffusivity. Equations (13) and (14) may be rewritten as:

$$m_\mathrm{p} c_\mathrm{p,i} \frac{\mathrm{d}T_\mathrm{p}}{\mathrm{d}t} = \pi d_\mathrm{V} \frac{Nu}{\Phi} (T_\mathrm{a} - T_\mathrm{p}) - \dot{m}_\mathrm{ev} L_\mathrm{v}(T_\mathrm{p}) - \dot{m}_\mathrm{sub} L_\mathrm{s}(T_\mathrm{p}) - \dot{m}_\mathrm{f} L_\mathrm{f}(T_\mathrm{p}) \tag{15}$$

$$\dot{m}_\mathrm{ev} = \pi d_\mathrm{V} \frac{Sh}{\Phi} \rho_\mathrm{a} D_\mathrm{v,a} (y_\mathrm{v,s}^\mathrm{liq}(T_\mathrm{p}, p_\mathrm{a}) - y_{\mathrm{v},\infty}) \tag{16a}$$

$$\dot{m}_\mathrm{sub} = \pi d_\mathrm{V} \frac{Sh}{\Phi} \rho_\mathrm{a} D_\mathrm{v,a} (y_\mathrm{v,s}^\mathrm{sol}(T_\mathrm{p}, p_\mathrm{a}) - y_{\mathrm{v},\infty}) \tag{16b}$$

In [22], using a Reynolds-type analogy, the following Nusselt and Sherwood correlations are proposed:

$$Nu(\Phi, Re_\mathrm{p}) = 2\sqrt{\Phi} + 0.55 Pr^{1/3} \Phi^{1/4} \sqrt{Re_\mathrm{p}} \tag{17}$$

$$Sh(\Phi, Re_\mathrm{p}) = 2\sqrt{\Phi} + 0.55 Sc^{1/3} \Phi^{1/4} \sqrt{Re_\mathrm{p}} \tag{18}$$

where P_r and S_c are respectively the Prandlt and Schmidt numbers. During the melting phase, the following set of equations is solved:

$$L_\mathrm{f}(T_\mathrm{f}) \frac{\mathrm{d}m_\mathrm{p,i}}{\mathrm{d}t} = -\dot{m}_\mathrm{f} L_\mathrm{f}(T_\mathrm{f}) = -\pi d_\mathrm{V} \frac{Nu}{\Phi} (T_\mathrm{a} - T_\mathrm{p}) + \dot{m}_\mathrm{ev} L_\mathrm{f}(T_\mathrm{f}) \tag{19}$$

$$\frac{\mathrm{d}m_\mathrm{p}}{\mathrm{d}t} = -\dot{m}_\mathrm{ev} = -\pi d_\mathrm{V} \frac{Sh}{\Phi} \rho_\mathrm{a} D_\mathrm{v,a} (y_\mathrm{v,s}^\mathrm{liq}(T_\mathrm{p}, p_\mathrm{a}) - y_{\mathrm{v},\infty}) \tag{20}$$

$$d_\mathrm{V} = \left[\frac{6}{\pi} \left(\frac{m_\mathrm{p} - m_\mathrm{p,i}}{\rho_\mathrm{w}} + \frac{m_\mathrm{p,i}}{\rho_\mathrm{p0}} \right) \right]^{1/3} \tag{21}$$

$$\frac{1}{\rho_{\mathrm{p}}} = \frac{1}{\rho_{\mathrm{p0}}}\frac{m_{\mathrm{p,i}}}{m_{\mathrm{p}}} + \frac{1}{\rho_{\mathrm{w}}}\left[1 - \left(\frac{m_{\mathrm{p,i}}}{m_{\mathrm{p}}}\right)\right] \tag{22}$$

$$\Phi = \left(\frac{m_{\mathrm{p,i}}}{m_{\mathrm{p}}}\right)\Phi_0 + \left[1 - \left(\frac{m_{\mathrm{p,i}}}{m_{\mathrm{p}}}\right)\right] \tag{23}$$

where Φ_0 denotes the value of the particle sphericity at the beginning of the melting phase, $m_{\mathrm{p,i}}$ is the ice core mass, ρ_{p0} and ρ_{w} are respectively the densities of the fully frozen snowflake (before the melting process starts) and liquid water. Equations (22) and (23) are replaced by:

$$\rho_{\mathrm{p}} = \rho_{\mathrm{p0}} + \left(\rho_{\mathrm{w}} - \rho_{\mathrm{p0}}\right)\left[1 - \exp\left(-2.55\frac{\mathrm{Y_w}}{1-\mathrm{Y_w}}\right)\right] \tag{24}$$

$$\Phi = \Phi_0 + (1 - \Phi_0)\left[1 - \exp\left(-2.55\frac{\mathrm{Y_w}}{1-\mathrm{Y_w}}\right)\right] \tag{25}$$

The justification of the form of Eq. (24) for particle density during melting is given in Sec. III.B.

2. Mitra's model [36]

The procedure described in the previous section is identical for the Mitra model. Equations (19) and (20) are replaced by the following equations :

$$L_{\mathrm{f}}(T_{\mathrm{f}})\frac{\mathrm{d}m_{\mathrm{p,i}}}{\mathrm{d}t} = -\dot{m}_{\mathrm{f}}L_{\mathrm{f}}(T_{\mathrm{f}}) = -4\pi f_{\mathrm{v}}C_{\mathrm{i}}(T_{\mathrm{a}} - T_{\mathrm{p}}) + \dot{m}_{\mathrm{ev}}L_{\mathrm{f}}(T_{\mathrm{f}}) \tag{26}$$

$$\frac{\mathrm{d}m_{\mathrm{p}}}{\mathrm{d}t} = -\dot{m}_{\mathrm{ev}} = -4\pi f_{\mathrm{v}}C_{\mathrm{i}}\rho_{\mathrm{a}}D_{\mathrm{v,a}}(y^{\mathrm{liq}}_{\mathrm{v,s}}(T_{\mathrm{p}}, p_{\mathrm{a}}) - y_{\mathrm{v},\infty}) \tag{27}$$

To derive this set of equations it is necessary to assume that thermal and mass diffusivities behave in the same way around the particle ($Pr = Sc$). The ventilation coefficient f_{v} is introduced for the steam heat and mass transfers as well as the capacitance of the melted flake C_{i} (see Pruppacher and Klett [2]). The ventilation coefficient is calculated using the Hall and Pruppacher correlation [37] which can be written as a function of $\chi = \frac{Re_p}{Sc}$:

$$f_v = \begin{cases} 1 + 0.14\chi^2, & \chi \leqslant 1.0 \\ 0.86 + 0.28\chi, & \chi \geqslant 1.0 \end{cases} \tag{28}$$

From the geometrical point of view the Mitra's model assumes an oblate spheroid for the idealized snowflake. The capacitance C_{i} is computed from the linear relation:

$$C_{\mathrm{i}} = (0.8 + 0.2Y_w)C_{\mathrm{i,0}} \tag{29}$$

where $Y_w = \frac{m_{\mathrm{p,w}}}{m_{\mathrm{p}}}$ is the water mass fraction. The initial capacitance of the snowflake $C_{\mathrm{i,0}}$ is given by :

$$C_{\mathrm{i,0}} = \frac{a_{\mathrm{i}}e}{sin^{-1}e}, \quad a_{\mathrm{i}} = \sqrt[3]{\frac{3m_{\mathrm{p,i}}}{4\pi(\mathrm{AR})_i\rho_{\mathrm{p}}}} \tag{30}$$

where $(\mathrm{AR})_i = \frac{c}{a}$ denotes the spheroid axis ratio. During the melting phase, Mitra assumes that $(\mathrm{AR})_i$ and ρ_{p} also vary linearly with respect to the water mass fraction Y_w according to the following relations:

$$(\mathrm{AR})_i = 0.3 + 0.7Y_w \tag{31}$$

$$\rho_{\mathrm{p}} = 20 + 980Y_w \tag{32}$$

III. Comparison between the experiments and the numerical simulations

In this section, comparisons between the numerical simulations and the experiments are proposed (free fall of a snowflake (section I.A.1) and particle melting (section I.A.2)). For the numerical simulations, the two drag models of Hölzer and Sommerfeld (H&S) (section II.A.1) and Heymsfield and Westbrook (H&W) (section II.A.2) are compared. For the melting experiment, the model based on the modified Nusselt and Sherwood numbers (Sec. II.B.1) and the Mitra's model (Sec. II.B.2) are evaluated.

A. Snowflake free fall velocity

Terminal free fall velocities for 17 snowflakes are mesured with the experimental method described in Sec. I.A.1. Conditions are described in Tab.1. Figure 8 shows the comparison between the experimental and numerical results for

N	Fall speed m/s	Mass mg	BL Mass mg	$d_{V,pro}$ mm	ρ_{pro} kg/m^3	ρ_{pro}(BL) kg/m^3	Φ_{pro} -	$\Phi^{\perp}_{pro}$ -	$d_{V,obl}$ mm	ρ_{obl} kg/m^3	ρ_{obl}(BL) kg/m^3	Φ_{obl} -	$\Phi^{\perp}_{obl}$ -	d_{max} mm	ρ_{max} kg/m^3	ρ_{max}(BL) kg/m^3	A_r -
1	0.67	0.063	0.105	1.042	117.0	180.0	0.95	1.05	1.248	64.8	103.2	0.93	1.51	1.505	38.1	62.4	0.34
2	1.83	1.480	0.924	2.571	192.5	100.2	0.95	1.02	3.098	102.1	56.2	0.93	1.51	3.745	55.2	32.4	0.45
3	2.40	16.790	3.907	4.977	265.0	61.1	0.96	1.08	5.880	158.4	36.7	0.95	1.51	6.953	95.4	22.2	0.43
4	1.47	0.576	0.532	2.340	97.2	83.8	0.98	1.47	2.599	65.9	58.1	0.97	1.82	2.898	45.6	41.3	0.47
5	1.49	0.132	0.155	1.143	174.1	195.5	0.98	1.11	1.263	131.1	145.9	0.98	1.35	1.396	99.2	109.3	0.57
6	1.44	0.546	1.217	3.018	40.4	83.6	0.98	1.14	3.369	28.3	59.5	0.98	1.42	3.763	19.9	42.7	0.56
7	1.07	0.170	0.314	1.653	75.1	135.8	0.98	1.09	1.882	51.8	93.2	0.97	1.42	2.144	35.9	64.3	0.49
8	1.80	0.298	0.236	1.493	184.6	138.2	0.97	1.26	1.672	124.2	95.2	0.97	1.56	1.880	86.7	68.3	0.52
9	0.92	0.047	0.085	0.862	188.0	265.7	0.92	0.82	1.075	83.3	127.5	0.90	1.25	1.352	40.8	66.8	0.51
10	1.38	0.243	0.528	2.109	54.7	108.5	0.98	1.12	2.330	38.1	78.0	0.98	1.37	2.583	27.1	57.6	0.56
11	1.69	0.459	0.515	1.994	113.1	125.0	0.97	1.04	2.317	75.6	82.6	0.96	1.39	2.697	51.6	55.7	0.47
12	1.28	0.157	0.191	1.300	168.5	168.0	0.94	0.92	1.591	81.8	87.4	0.92	1.40	1.957	41.2	47.5	0.42
13	1.49	0.134	0.148	1.127	227.4	199.8	0.93	0.87	1.407	109.4	100.4	0.91	1.37	1.766	54.3	52.2	0.57
14	1.64	0.349	0.246	1.487	203.4	143.1	0.98	1.10	1.644	150.9	106.1	0.98	1.35	1.818	112.0	78.7	0.59
15	1.41	0.578	0.582	2.150	178.1	111.2	0.98	1.13	2.386	130.9	81.7	0.98	1.39	2.648	96.2	60.0	0.59
16	1.51	0.266	1.201	3.195	18.5	71.4	0.95	1.15	3.728	10.3	42.5	0.94	1.58	4.391	6.1	27.4	0.36
17	1.21	0.150	0.482	2.017	38.9	114.3	0.97	1.10	2.296	24.1	74.9	0.96	1.43	2.628	15.8	51.7	0.45

Table 1 Snowflake free fall study. Experimental data.

the snowflake terminal velocity. Different models for the drag coefficient are compared (H&S and H&W) as well as different definition for the spheroid reconstruction (prolate or oblate) in the case of the H&S drag model. The mass of the snowflakes used in Eq. (2) is given by the experiments. Each snowflake being described by three views (front, side and bottow, Sec. I.A.1), the inputs for the snowflake geometric description (reference surface A_{ref} and oblate/prolate spheroid reconstruction) are obtained by the arithmetic average of the input data measured from the three views. Both H&S and H&W models are able to reproduce the terminal free fall velocity with a relative accuracy of 30%. Regarding H&S model, the spheroid reconstruction (prolate or oblate) has a small influence on the terminal velocity. Thus, drag models validated for higher density ice crystals (ρ_p = 917 kg.m^{-3} [22]) remain valid for snowflakes by defining the particle density as a lower bulk density built from a convex geometric volume enveloping the particle as a prolate/oblate spheroid.

In Tab. 2, the relative errors between the numerical and experimental velocities are shown when only one view is used for the snowflake geometric description (either front, side or bottom), without averaging among the three views. The error does not depend on the chosen view, which validates the average procedure over the three views used in Fig. 8

L2 Relative error w.r.t experimental fall velocity	**H&S prolate**	**H&S oblate**	**H&W**
Front view	0.21	0.20	0.19
Side view	0.20	0.20	0.20
Bottom view	0.24	0.23	0.23

Table 2 Relative error between numerical and experimental terminal velocities. Only one view is used for the snowflake geometric description (either front, side or bottom).

and the absence of a privileged direction of the particle during the free fall.

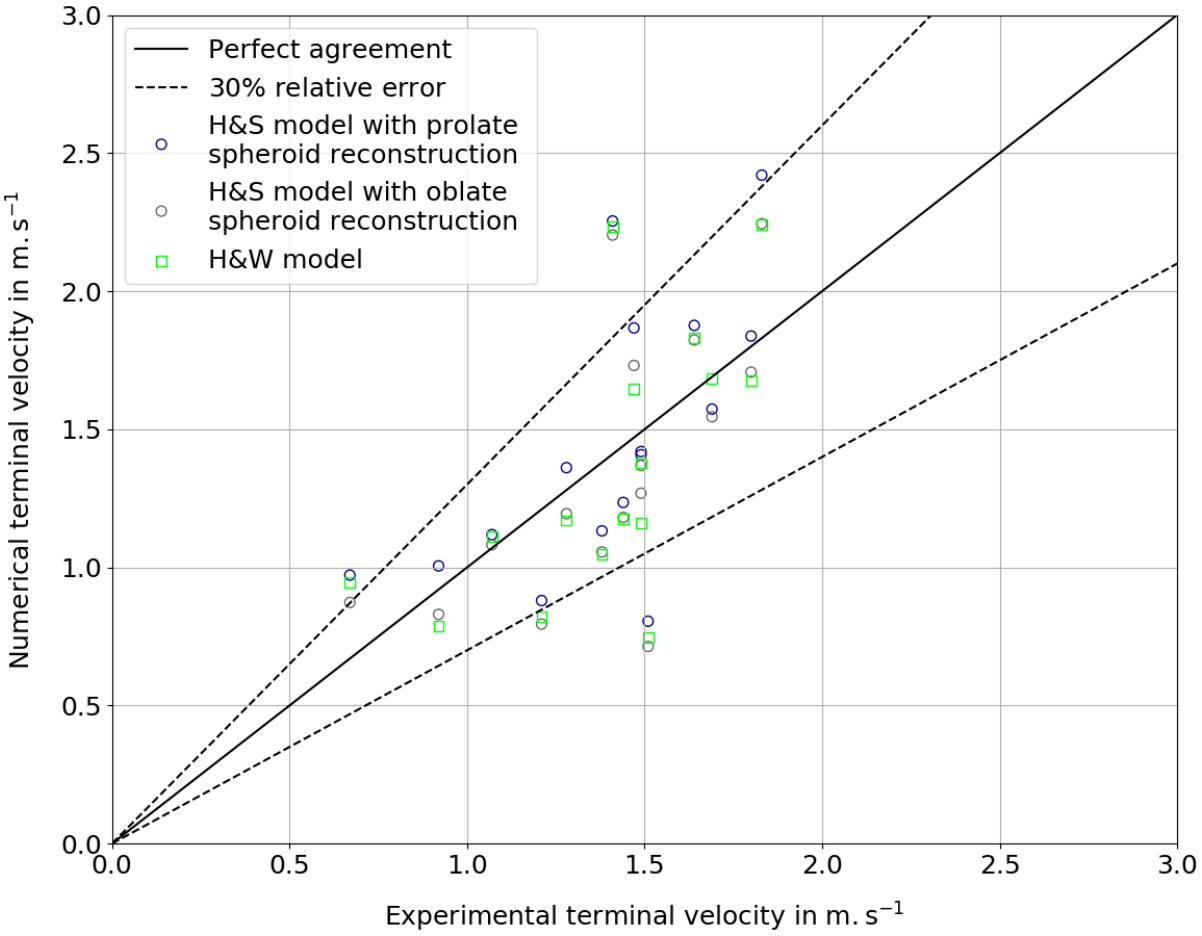

Fig. 8 Snowflake free fall velocity. Comparison between the experimental (abscissa) and numerical (ordinate) results for the snowflake terminal velocity (see Tab. 1 for the test case description). Main diagonal means a perfect agreement. ± 30% relative error regions are shown. Different models are compared to evaluate the drag coefficient (H&S and H&W) as well as different definition for the spheroid reconstruction (prolate or oblate) in the case of the H&S drag model. The mass of the snowflakes used in Eq. (2) is given by the experiments.

B. Snowflake melting

Melting times for 7 snowflakes are measured with the experimental method described in Sec. I.A.2. Conditions are described in Tab. 3.

N	Melting time s	mass mg	BL mass mg	Air Temp. K	Air speed m/s	RH -	$d_{V,pro}$ mm	ρ_{pro} kg/m^3	ρ_{pro}(BL) kg/m^3	Φ_{pro} -	$d_{V,obl}$ mm	ρ_{obl} kg/m^3	ρ_{obl}(BL) kg/m^3	Φ_{obl} -	d_{max} mm	ρ_{max} kg/m^3	ρ_{max}(BL) kg/m^3	A_r -
1	17.1	0.972	0.418	308.9	1.02	0.04	2.147	187.5	80.7	0.9	3.061	64.7	27.9	0.8	4.363	22.3	9.6	0.3
2	9.2	0.396	0.189	309.1	1.02	0.11	1.432	257.7	122.8	0.8	2.295	62.6	29.8	0.7	3.677	15.2	7.2	0.2
3	15.1	0.723	0.304	301.5	1.02	0.06	1.761	252.8	106.4	1.0	2.115	145.9	61.4	0.9	2.541	84.2	35.4	0.4
4	8.0	0.318	0.152	306.2	0.88	0.04	1.231	325.2	155.6	0.9	1.614	144.4	69.1	0.9	2.116	64.1	30.7	0.4
5	4.4	0.106	0.085	308.4	0.88	0.02	1.123	142.2	114.9	0.9	1.417	70.8	57.2	0.9	1.788	35.3	28.5	0.3
6	10.1	0.240	0.122	305.5	0.88	0.01	1.195	268.7	136.9	0.9	1.514	132.2	67.4	0.9	1.918	65.0	33.1	0.4
7	6.2	0.228	0.142	310.1	0.88	0.02	1.236	230.3	144.1	1.0	1.414	153.9	96.3	1.0	1.617	102.8	64.3	0.5

Table 3 Snowflake melting study. Experimental data.

First, the evolution of the snowflake density during the melting process is studied. In Fig. 9, time evolution of the density of snowflake N^{o}3 from Tab. 3 is shown. Blue symbols represent the densities ρ_p obtained from the ratio

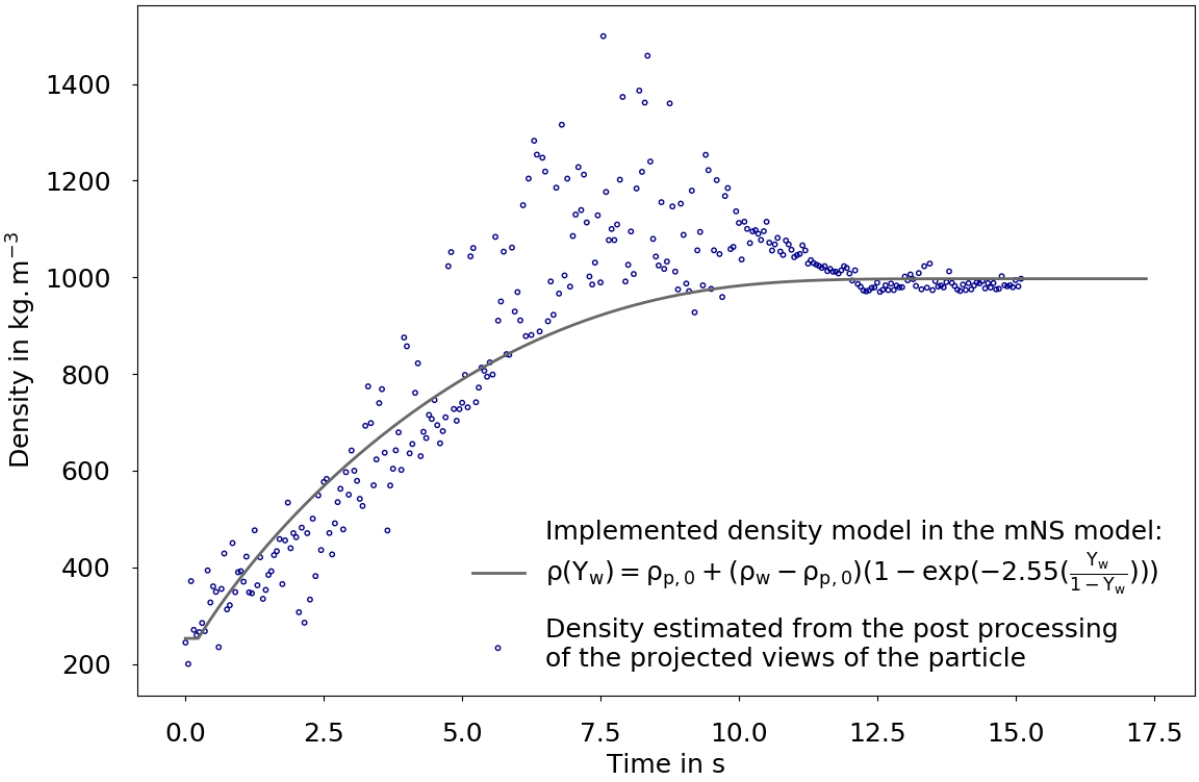

Fig. 9 Time evolution of the density of snowflake N^{o}3 from Tab. 3. Blue symbols represent the densities $\rho_\mathbf{p}$ obtained from the ratio $\rho_\mathbf{p} = m_\mathbf{p}/V_\mathbf{spheroid}$. The volume $V_\mathbf{spheroid}$ is estimated from the post processing of the projected views of the particle described in Sec. I.B (prolate reconstruction). The mass of the particle $m_\mathbf{p}$ is assumed to be constant along the trajectory (mass loss due to evaporation neglected). It is estimated from the final spherical shape of the liquid droplet once the whole snowflake is melted. In the model's formulation (black solid line), $\rho_\mathbf{p,0}$ stands for the initial density of the fully glaciated snowflake while $\rho_\mathbf{w}$ is the liquid water density.

$\rho_\mathrm{p} = m_\mathrm{p}/V_\mathrm{spheroid}$. The volume V_spheroid is estimated from the post processing of the projected views of the particle described in Sec. I.B (prolate reconstruction). The mass of the particle m_p is assumed to be constant along the trajectory (mass loss due to evaporation neglected). It is estimated from the final spherical shape of the liquid droplet once the whole snowflake is melted. For intermediate times (6s $\leq t \leq$ 11s), the reconstructed value for ρ_p is larger than ρ_w, the limit value of the density of the final spherical liquid droplet. This may be explained by Fig. 10 where the projected views of the particle used to reconstruct the prolate V_spheroid (Sec. I.B) are shown for different times. The ratio $V_\mathrm{spheroid}/V_\mathrm{ref}$ is specified, where V_ref is the volume of the final spherical liquid droplet once the whole snowflake is melted. The left column represents the digitized pictures from the grayscale images generated by the experiments (right column). At times 7.50s and 7.55s, which belong to the time interval where $V_\mathrm{spheroid} < V_\mathrm{ref}$ (or equivalently $\rho_\mathrm{p} > \rho_\mathrm{w}$, Fig. 9), the particle is not yet fully melted or spherical. However it is relatively compact and close to a sphere. Thus, given the small gap between V_spheroid and V_ref, the error due to the 2D/3D geometric reconstruction may allow values of V_spheroid smaller than V_ref, and thus $\rho_\mathrm{p} > \rho_\mathrm{w}$. At shorter times ($t <$ 5s), the difference between V_spheroid and V_ref is greater than the difference between the exact volume of the particle and the reconstructed volume V_spheroid from the 2D projected view. Finally, the following law is chosen for the particle density during the melting process (mNS model):

$$\rho_\mathrm{p}\left(\mathrm{Y_w}\right) = \rho_\mathrm{p0} + \left(\rho_\mathrm{w} - \rho_\mathrm{p0}\right)\left[1 - \exp\left(-\beta\frac{\mathrm{Y_w}}{1-\mathrm{Y_w}}\right)\right] \tag{33}$$

where ρ_p0 is the density of the fully frozen snowflake (before the melting process starts) and β a constant to be adjusted. From Fig. 9, a minimization procedure leads to $\beta = 2.55$.

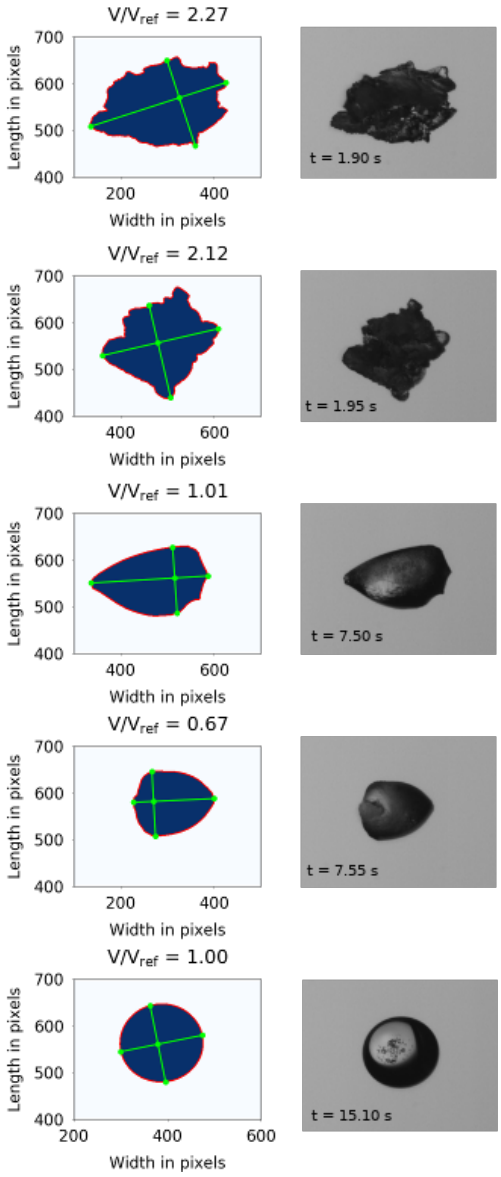

Fig. 10 For snowflake N^{o}3 (Tab. 3), projected views of the particle used to reconstruct the prolate V_{spheroid} (Sec. I.B) at different times. The ratio $V_{\text{spheroid}}/V_{\text{ref}}$ is specified, where V_{ref} is the volume of the final spherical liquid droplet once the whole snowflake is melted. Left column: digitized pictures from the grayscale images generated by the experiments (right column).

Figure 11 shows a comparison between the experimental and numerical results for snowflake melting times. The model based on the modified Nusselt and Sherwood numbers (referred to as mNS model, Sec. II.B.1) and the Mitra's model (Sec. II.B.2) are compared. For the mNS model, different definitions for the spheroid reconstruction (prolate or oblate) are proposed. The mass of the snowflakes used in Eq. (13) is given by the experiments. For every snowflake, the results are shown for each view (front, side or bottom). Both models are able to compute the melting time with a relative accuracy of 30%. Regarding the mNS model, the spheroid reconstruction (prolate or oblate) has a small influence on the final melting time.

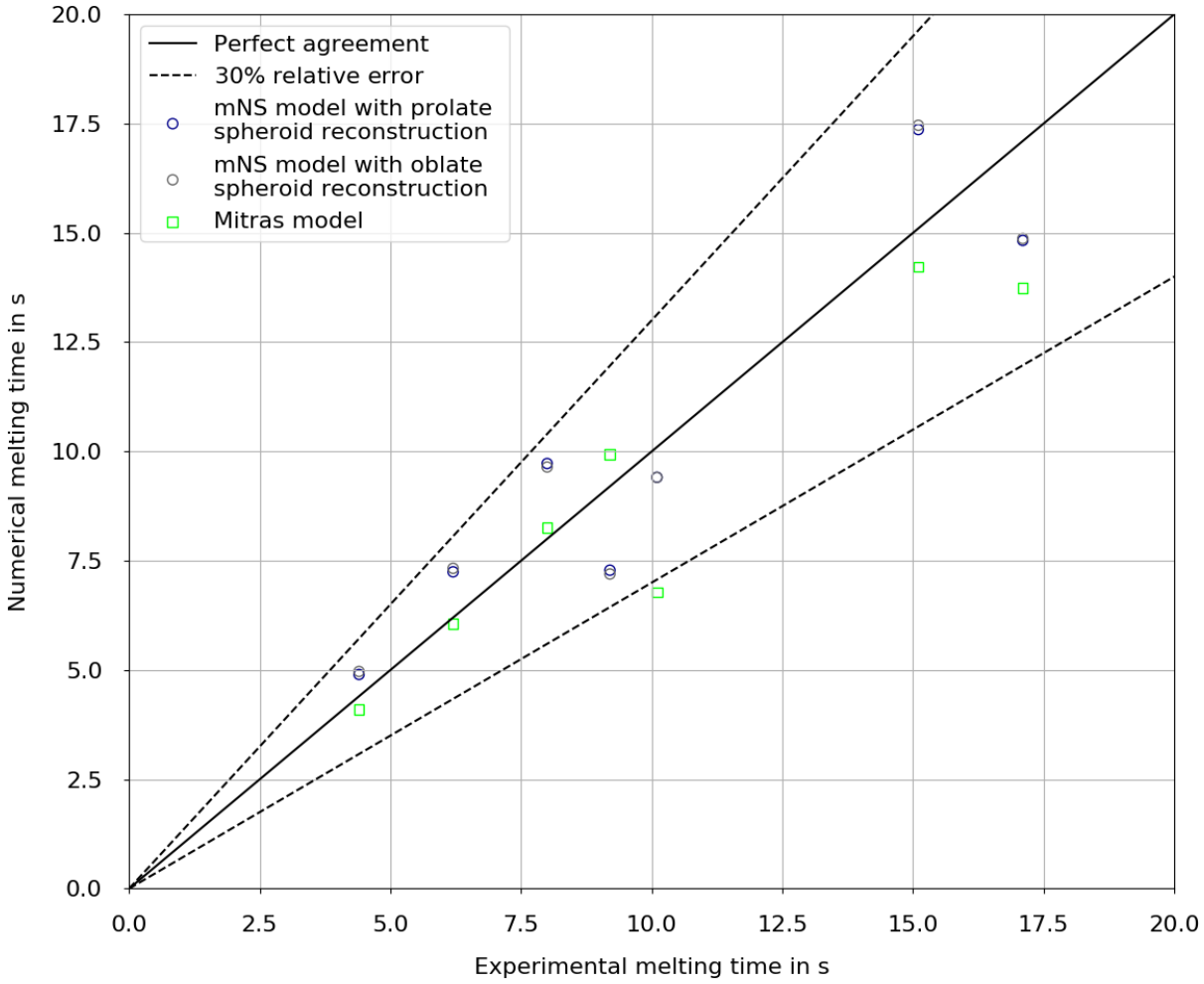

Fig. 11 Snowflake melting time. Comparison between the experimental (abscissa) and numerical (ordinate) results for the snowflake melting time (see Tab. 3 for the test case description). Main diagonal means a perfect agreement. ± 30% relative error regions are shown. The model based on the modified Nusselt and Sherwood numbers (referred to as mNS model, Sec. II.B.1) and the Mitra's model (Sec. II.B.2) are compared. For the mNS model, different definitions for the spheroid reconstruction (prolate or oblate) are proposed. The mass of the snowflakes used in Eq. (13) **is given by the experiments.**

C. Mass-diameter model for mass estimation

So far, it has been assumed that the mass of the snowflakes is known as an experimental input for the experiments dedicated to snowflake free fall velocity and melting times. We are now interested in the impact of using a mass-diameter correlation to predict snowflake mass. The Baker and Lawson relationship is used [28]. It is based on the two Feret diameters f_{max} and $f^{\perp}_{max}$ (Sec. I.B) and allows the estimation of the mass of the particle using only one single view. It is defined as:

$$BL_{mass} = 0.135 CSP^{0.793}, \quad CSP = \frac{A^{\perp} f^{\perp}_{max}(2f_{max} + 2f^{\perp}_{max})}{P} \tag{34}$$

where P denotes the perimeter and $A^{\perp}$ the projected area of the particle (in the considered view).

Figure 12 shows a comparison between the measured experimental mass of the snowflake and the mass derived from the Baker and Lawson mass-diameter correlation. Data from both the snowflake terminal fall velocity and the melting time experiments are shown. Note that, for a given particle, the differences observed between the mass estimated by the Baker and Lawson mass-diameter correlation and the reference mass given by the experiments amount to defining

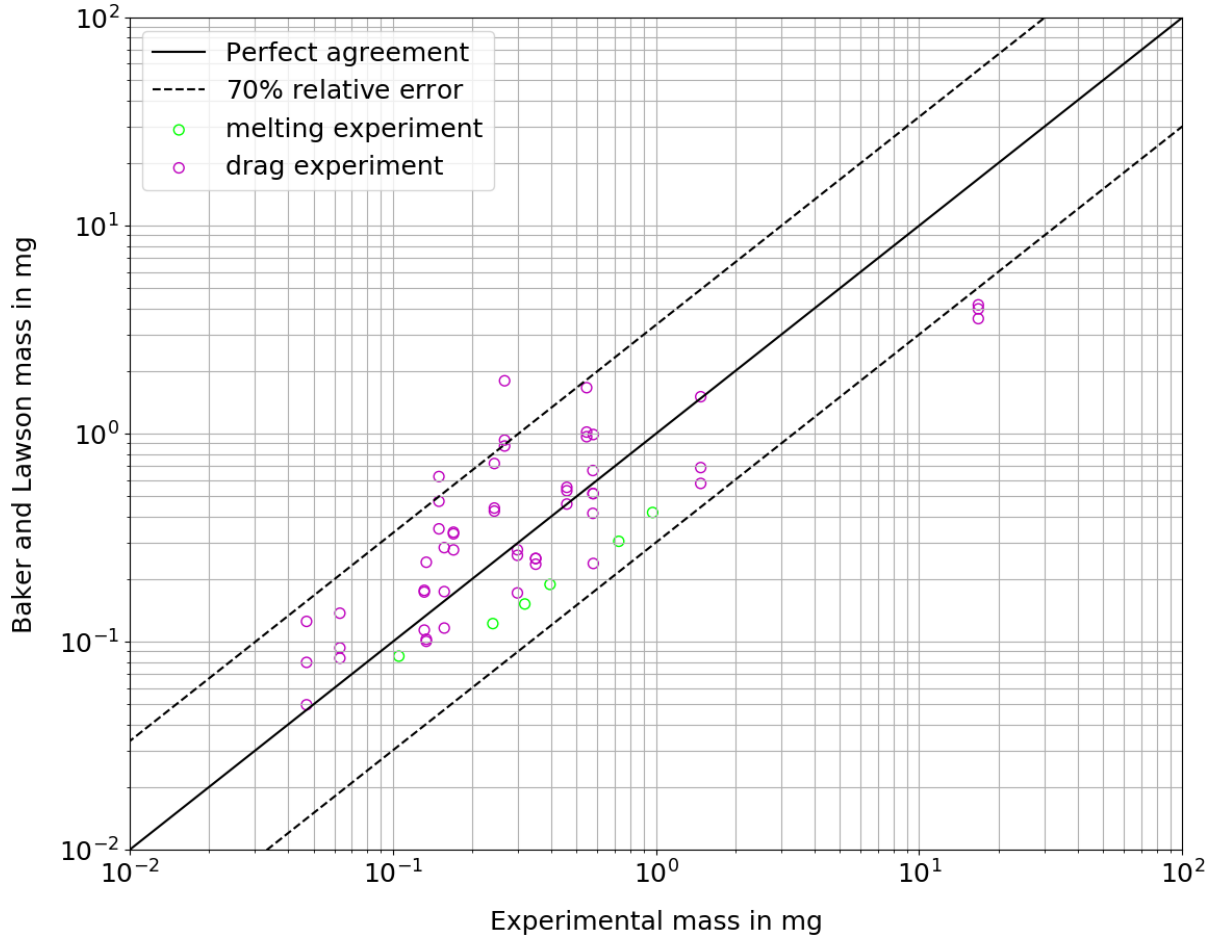

Fig. 12 Comparison between the measured experimental mass of the snowflake (abscissa) and the mass derived from the Baker and Lawson mass-diameter correlation (ordinate). Main diagonal means a perfect agreement. Data from both the snowflake terminal fall velocity and the melting time experiments are shown.

a different bulk density for the particle since the calculated volume remains the same (based on the same spheroid reconstruction). For a given volume, using the Baker and Lawson law for the particle mass is therefore equivalent to making an average error of 70% on the bulk density.

Figure 13 shows the influence of the use of the Baker and Lawson mass-diameter correlation on the particle's dynamics and thermics. Figure 13a focuses on the estimation of the particle terminal free fall velocity. The use of an approximated value for the particle mass does not induce additional errors on the estimation of the terminal velocity. This has to be confirmed for more realistic trajectories and not only for terminal fall velocities.

Regarding melting times (Fig. 13b), the use of the Baker and Lawon law for the particle mass leads to an underestimation of the snowflake melting time. Thermal behavior of the particle seems to be sensitive to its bulk density.

Conclusions

In the framework of the modeling of snowflake trajectory and heat and mass transfers, a method for reconstructing the volume input parameters of the models has been proposed. It is based on image post-processing and allows to build a convex hull around the particle defined by a prolate or oblate spheroid. Volume reconstruction is possible from a single view of the snowflake. This leads to a definition for the snowflake bulk density much smaller than the densities usually used for ice particles. The approach is validated with two experiments, namely the estimation of the terminal free fall velocity of a snowflake and the typical melting times. Different models from the literature are tested to evaluate

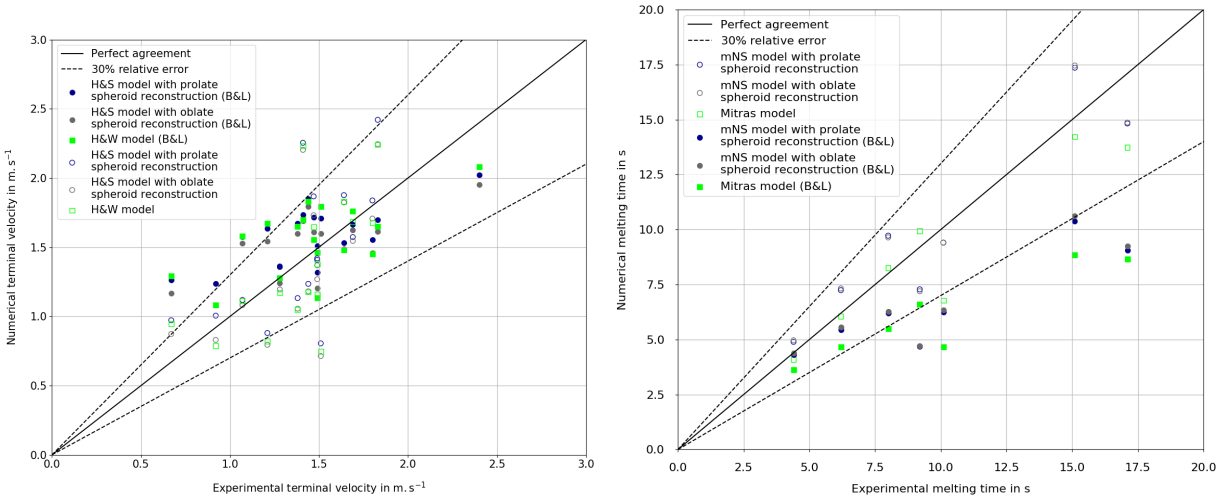

(a) Snowflake terminal free fall velocity experiment

(b) Snowflake melting time experiment

Fig. 13 Influence of the use of the Baker and Lawson (B&L) mass-diameter correlation on the particle's dynamics and thermics.

the drag coefficient and heat and mass transfers during the melting process. Provided that the snowflake mass is known accurately, the predictions for the terminal fall velocity and the melting time are acceptable. Discrepancies appear when a correlation is used to evaluate the mass of the snowflake (typically a mass-diameter correlation). This has to be improved in future works.

Acknowledgments

The funding from the European Union's Horizon 2020 research and innovation programme under grant agreement No 824310 is gratefully acknowledged.

References

[1] Nakaya, U., and Terada, T., "Simultaneous observations of the mass, falling velocity and form of individual snow crystals," *J. of the Faculty of Science, Hokkaido Imperial University*, Vol. 1, No. 7, 1935, pp. 191–200.

[2] Pruppacher, H., and Klett, J., "Microphysics of clouds and precipitation," *Nature*, Vol. 284, No. 5751, 1980, pp. 88–88.

[3] Garrett, T., Fallgatter, C., Shkurko, K., and Howlett, D., "Fall speed measurement and high-resolution multi-angle photography of hydrometeors in free fall," *Atmos. Meas. Tech*, Vol. 5, No. 11, 2012, pp. 2625–2633.

[4] Dezitter, F., Grandin, A., Brenguier, J.-L., Hervy, F., Schlager, H., Villedieu, P., and Zalamansky, G., "HAIC-High Altitude Ice Crystals," *5th AIAA Atmospheric and Space Environments Conference*, 2013, p. 2674.

[5] Villedieu, P., Trontin, P., Aouizerate, G., Bansmer, S., Vanacore, P., Roisman, I., and Tropea, C., "MUSIC-haic: 3D multidisciplinary tools for the simulation of in-flight icing due to high altitude ice crystals." *SAE Int. J. Adv. & Curr. Prac. in Mobility*, Vol. 2, No. 1, 2020, pp. 78–89.

[6] Hauk, T., "Investigation of the Impact and Melting Process of Ice Particles," Ph.D. thesis, T.U. Darmstadt, 2016.

[7] Kintea, D., "Hydrodynamics and Thermodynamics of Ice Particle Accretion," Ph.D. thesis, T.U. Darmstadt, 2016.

[8] Baumert, A., "Experimental and numerical studies on ice crystal icing of civil aircraft," Ph.D. thesis, T.U. Braunschweig, 2019.

[9] Hauk, T., Bonaccurso, E., Villedieu, P., and Trontin, P., "Theoretical and Experimental Investigation of the Melting Process of Ice Particles," *J. of Thermophysics and Heat Transfer*, Vol. 30, No. 4, 2016, pp. 946–954.

[10] Kintea, D., Hauk, T., Roisman, I., and Tropea, C., "Shape evolution of a melting nonspherical particle," *Phys. Rev. E*, Vol. 92, No. 3, 2015, p. 033012.

[11] Baumert, A., Bansmer, S., Trontin, P., and Villedieu, P., "Experimental and numerical investigations on aircraft icing at mixed phase conditions," *Int. J. Heat Mass Transfer*, Vol. 123, 2018, pp. 957–978.

[12] Trontin, P., Blanchard, G., and Villedieu, P., "A comprehensive numerical model for mixed-phase and glaciated icing conditions," *8th AIAA Atmospheric and Space Environments Conference*, 2016, p. 3742.

[13] Aouizerate, G., Charton, V., Balland, M., Senoner, J., Trontin, P., Laurent, C., Blanchard, G., and Villedieu, P., "Ice crystals trajectory calculations in a turbofan engine." *10th AIAA Atmospheric and Space Environments Conference, AIAA Aviation, AIAA-2018-4130, Atlanta, USA*, 25-29 June 2018.

[14] Trontin, P., and Villedieu, P., "A comprehensive accretion model for glaciated icing conditions," *Int. J. of Mult. Flow.*, Vol. 108, 2018, pp. 105–123.

[15] Norde, E., Senoner, J., van der Weide, E., Trontin, P., Hoeijmakers, H., and Villedieu, P., "Eulerian and Lagrangian Ice Crystal Trajectory Simulations in a Generic Turbofan Compressor," *J. Prop. Power*, Vol. 35, No. 1, 2019, pp. 26–40.

[16] Hauk, T., Bonaccurso, E., Roisman, I., and Tropea, C., "Ice crystal impact onto a dry solid wall. Particle fragmentation," *Proc. R. Soc. A*, Vol. 471, No. 2181, 2015, p. 20150399.

[17] Roisman, I., and Tropea, C., "Impact of a crushing ice particle onto a dry solid wall," *Proc. R. Soc. A*, Vol. 471, No. 2183, 2015, p. 20150525.

[18] Kintea, D., Breitenbach, J., Thammanna Gurumurthy, V., Roisman, I., and Tropea, C., "On the influence of surface tension during the impact of particles on a liquid-gaseous interface," *Phys. of Fluids*, Vol. 28, No. 1, 2016, p. 012108.

[19] Kintea, D., Hauk, T., Breitenbach, J., Roisman, I., and Tropea, C., "Oblique water entry of rigid spheres," *ILASS–Europe 2014, 26th Annual Conference on Liquid Atomization and Spray Systems*, 2014.

[20] Kintea, D., Roisman, I., and Tropea, C., "Transport processes in a wet granular ice layer: Model for ice accretion and shedding," *Int. J. of Heat and Mass Transfer*, Vol. 97, 2016, pp. 461–472.

[21] Kintea, D., Schremb, M., Roisman, I., and Tropea, C., "Numerical investigation of ice particle accretion on heated surfaces with application to aircraft engines," *11th AIAA/ASME Joint Thermophysics and Heat Transfer Conference, AIAA-2014-2820*, 2014.

[22] Villedieu, P., Trontin, P., and Chauvin, R., "Glaciated and mixed phase ice accretion modeling using ONERA 2D icing suite," *6th AIAA atmospheric and space environments conference*, 2014, p. 2199.

[23] Huet, F., "Description and Overview of the ICE GENESIS Research Project," *International Conference on icing, SAE 2019, Minneapolis,USA*, 2019.

[24] Hölzer, A., and Sommerfeld, M., "New simple correlation formula for the drag coefficient of non-spherical particles," *Powder Technology*, Vol. 184, No. 3, 2008, pp. 361–365.

[25] Heymsfield, A. J., and Westbrook, C., "Advances in the estimation of ice particle fall speeds using laboratory and field measurements," *Journal of the Atmospheric Sciences*, Vol. 67, No. 8, 2010, pp. 2469–2482.

[26] Haider, A., and Levenspiel, O., "Drag coefficient and terminal velocity of spherical and nonspherical particles," *Powder technology*, Vol. 58, No. 1, 1989, pp. 63–70.

[27] Ganser, G. H., "A rational approach to drag prediction of spherical and nonspherical particles," *Powder technology*, Vol. 77, No. 2, 1993, pp. 143–152.

[28] Baker, B., and Lawson, R. P., "Improvement in determination of ice water content from two-dimensional particle imagery. Part I: Image-to-mass relationships," *Journal of applied meteorology and climatology*, Vol. 45, No. 9, 2006, pp. 1282–1290.

[29] Abraham, F. F., "Functional dependence of drag coefficient of a sphere on Reynolds number," *The Physics of Fluids*, Vol. 13, No. 8, 1970, pp. 2194–2195.

[30] Böhm, H. P., "A general equation for the terminal fall speed of solid hydrometeors," *Journal of the Atmospheric Sciences*, Vol. 46, No. 15, 1989, pp. 2419–2427.

[31] Heymsfield, A. J., and Kajikawa, M., "An improved approach to calculating terminal velocities of plate-like crystals and graupel," *Journal of the atmospheric sciences*, Vol. 44, No. 7, 1987, pp. 1088–1099.

[32] Khvorostyanov, V. I., and Curry, J. A., "Terminal velocities of droplets and crystals: Power laws with continuous parameters over the size spectrum," *Journal of the atmospheric sciences*, Vol. 59, No. 11, 2002, pp. 1872–1884.

[33] Khvorostyanov, V. I., and Curry, J. A., "Fall velocities of hydrometeors in the atmosphere: Refinements to a continuous analytical power law," *Journal of the atmospheric sciences*, Vol. 62, No. 12, 2005, pp. 4343–4357.

[34] Mitchell, D. L., "Use of mass-and area-dimensional power laws for determining precipitation particle terminal velocities," *Journal of the atmospheric sciences*, Vol. 53, No. 12, 1996, pp. 1710–1723.

[35] Mitchell, W. F., and Tiesinga, E., "Adaptive grid refinement for a model of two confined and interacting atoms," *Applied numerical mathematics*, Vol. 52, No. 2-3, 2005, pp. 235–250.

[36] Mitra, S., Vohl, O., Ahr, M., and Pruppacher, H., "A wind tunnel and theoretical study of the melting behavior of atmospheric ice particles. IV: Experiment and theory for snow flakes," *Journal of the Atmospheric Sciences*, Vol. 47, No. 5, 1990, pp. 584–591.

[37] Hall, W., and Pruppacher, H., "The survival of ice particles falling from cirrus clouds in subsaturated air," *Journal of Atmospheric Sciences*, Vol. 33, No. 10, 1976, pp. 1995–2006.